

22 **Abstract.** Using the vertical velocity (w) observed by a Ka-band millimeter wave cloud radar (MMCR)
23 at Wuhan, we investigate the evolution of convective boundary layer height (CBLH) based on a specified
24 threshold of vertical velocity variance (σ_w^2). By comparison, the MMCR-derived CBLH is generally in good
25 agreement with that retrieved from the lidar range corrected signal (RCS), except for a few hours
26 post-sunrise and pre-sunset due to the influence of aerosol residual layer on the lidar RCS. Meanwhile, the
27 CBLH estimated from the MMCR σ_w^2 shows less contamination by passing sand and dust, and thick
28 high-level clouds due to the rapid response of aerosol w relative to its concentration, thus the MMCR
29 measurement can capture the diurnal evolution of CBLH. The MMCR observation in 2020 depicts the
30 diurnal evolution of seasonal and monthly mean CBLHs. The seasonal mean CBLH reaches the peak
31 heights of 1.29 km in summer, 1.14 km in spring, 0.66 km in autumn, and 0.6 km in winter, indicating the
32 dominant effect of radiation heating. The maximum value of monthly mean CBLH rises steadily from 0.66
33 km in January to 1.47 km July, followed by a gradual decline to 0.42 km in December. Statistical standard
34 deviations are monthly-dependent, showing the significant influence of weather conditions on the CBLH.
35 This study improves our understanding of the Ka-band MMCR's capability to monitor the evolution of
36 CBLH and track the dynamical processes in the CBL.

37

38 1. Introduction

39 The planetary boundary layer (PBL) is located in the lower part of the troposphere, and is where the
40 air-land (or air-sea) interaction takes place, thus the PBL is directly impacted by the surface forcings (Stull,
41 1988). Owing to the combined effects of friction, evaporation and transpiration, heat transfer, and pollutant
42 emission, the PBL is characterized by complex dynamical processes, with the prominent turbulence features
43 of vorticity and compressibility (Bernardini et al., 2012; Schneider, 2008). The height of PBL varies with
44 local time, ranging generally from a few tens of meters to several kilometers at mid latitudes. Since the PBL

45 regulates the exchange of momentum, moisture and mass between the ground and the free atmosphere
46 (Mahrt, 1999; Holtslag and Nieuwstadt, 1986), the structure of PBL is an important input variable in
47 numerical weather-prediction and climate models (Edwards et al., 2020).

48 The convective boundary layer (CBL) is a type of PBL driven primarily by convection, and the CBL
49 height (CBLH) has a distinct daily cycle. Convective sources include heat transfer from the ground surface
50 warmed by solar radiation, and radiative cooling-induced air sinking from the cloud top, thus the evolution
51 of CBL is mainly dominated by surface sensible heat, which is significantly influenced by weather
52 conditions, such as clouds, and humidity near the surface (Kwon et al., 2022; Ribeiro et al., 2018; Zhang et
53 al. 2014). On a clear day, the CBLH rises after sunrise and reaches its maximum in the afternoon (LeMone
54 et al., 2010; Grossman and Robert, 2005; Yates et al., 2001). When the CBL collapses after sunset, most of
55 aerosol particles within the CBL are deposited into the nocturnal stable PBL due to the rapid weakening of
56 convectively driven turbulence, and some particles are transformed into an aerosol residual layer. The
57 residual layer descends gradually due to the sinking effect until it is mixed with the CBL driven by the next
58 day's post-sunrise convection (Blay-Carreras et al., 2014; Heus et al., 2010; Tennekes and Driedonks, 1981).
59 At the CBL top, moisture, aerosols and other chemical substances can be entrained to the free atmosphere,
60 leading to an entrainment transition zone between the CBL and the free atmosphere (Franck et al., 2021; Liu
61 et al., 2021; Brooks and Fowler, 2007). Hence, the CBL has an influence not only on the dispersion of
62 surface emissions and pollutants (Kong and Yi, 2015; Pal et al., 2015; Stull, 1988), but also on the weather
63 processes above it through the entrainment process (Guo et al., 2017; Brooks and Fowler, 2007; Neggers et
64 al., 2004).

65 The observations of in situ radiosonde and remote sensing are extensively used to estimate the CBLH
66 and its seasonal features. Radiosonde can obtain many meteorological parameters with high precision,
67 providing the possibility of retrieving the CBLH through different algorithms (Seidel et al., 2010; Seibert,

68 2000). Typically, the vertical gradients of potential temperature and water vapor (including relative humidity
69 and specific humidity) are used to determine the CBLH (Zhang et al., 2022; Guo et al., 2021; Dang et al.,
70 2019; Liu and Liang, 2010; Seidel et al., 2010). Additionally, the CBL top can be evaluated using the
71 profiles of refractivity and bulk Richardson number derived from the temperature, pressure, vapor pressure
72 and horizontal wind data (Burgos-Cuevas et al., 2021; Guo et al., 2016; Zhang et al., 2014; Seidel et al.,
73 2012; Basha and Ratnam, 2009). These retrieval algorithms provide insights into the features of CBL from
74 the perspective of energy exchange, mass transport, turbulent motion and effect on radio propagation. Even
75 so, radiosonde faces a severe limitation in capturing the clear development of CBL due to its conventional
76 release schedule, which typically occurs only twice a day.

77 In contrast to radiosonde, ground-based remote sensing offers high temporal resolution in observational
78 profiles, which is essential to investigate the diurnal evolution of CBL. The vertical gradients in temperature,
79 humidity and turbulence change the profile of atmospheric refractive index, which can cause the scattering
80 of electromagnetic waves. Wind profile radar obtains the atmospheric wind speed and direction by
81 decomposing the Doppler shift of backscattered waves (Liu et al., 2020; Singh et al., 2016; Seibert, 2000).
82 In this way, several parameters from the wind profile radar measurement, such as signal-to-noise ratio,
83 Doppler spectral width, and refractive index structure constant, are utilized to retrieve the CBLH for every
84 30-60 minutes based on their vertical gradients or chosen thresholds (Burgos-Cuevas et al., 2023; Bianco et
85 al., 2022; Solanki et al., 2021; Liu et al., 2020; Allabakash et al., 2017; Sandeep et al., 2014). Nevertheless,
86 previous studies showed that the top of CBL derived from the radar observation may be influenced by strong
87 residual layer and shallow or large entrainment zone (Sandeep et al., 2014; Bianco and Wilczak, 2002).

88 Lidar is regarded as a powerful detection equipment for capturing the CBL development due to its high
89 sensitivity to echo signals from various atmospheric components. Its relatively short operating wavelength
90 allows it to receive echoes backscattered not only from aerosol and cloud particles, but also from

91 atmospheric molecules. Nevertheless, since Rayleigh scattering of atmospheric molecules is much weaker
92 than Mie scattering of aerosol particles, the profile of lidar backscatter coefficient or range corrected signal
93 (RCS) from aerosols is applied to determining the CBLH by tracing the height where the aerosol
94 concentration sharply decreases with height. Accordingly, many techniques have been developed to identify
95 the extreme value of RCS gradient (Liu et al., 2021; Su et al., 2020; Dang et al., 2019; Yang et al., 2017;
96 Granados-Muñoz et al., 2012). As a simplified low-power lidar, ceilometer is initially designed to measure
97 the height of cloud base, thus similarly, the backscatter profile in the ceilometer observation can be
98 employed in the CBL investigation (Zhang et al., 2022; Schween et al., 2014; Van Der Kamp and McKendry,
99 2010). However, due to the incapability of lasers to penetrate clouds, the CBLH may be contaminated and
100 even misinterpreted by clouds within the CBL in the lidar and ceilometer measurements (Schween et al.,
101 2014).

102 With the advances in atmospheric sounding technology, the vertical velocity from Doppler lidar provides
103 a direct estimation of CBLH, which can reduce the impact of strong aerosol concentration within the
104 residual layer on the retrieved CBLH (Burgos-Cuevas et al., 2023; Dewani et al., 2023; Huang et al., 2017;
105 Schween et al., 2014; Barlow et al., 2011). At the initial stage of CBL formation in the morning and the
106 rapid decline stage of CBL in the late afternoon (Dewani et al., 2023; Manninen et al., 2018; Schween et al.,
107 2014; Barlow et al., 2011), aerosol particles in the residual layer may cause the CBLH to be overestimated
108 several hundred meters. This discrepancy is due to aerosols from a long time-mixing process rather than the
109 current situation of convectively driven turbulence (Burgos-Cuevas et al., 2023; Schween et al., 2014;
110 Pearson et al., 2010). When utilizing Doppler lidar data, a specified threshold of vertical velocity variance is
111 used to define the height of CBL top. This method has been validated by comparison with the radiosonde
112 observation (Dang et al., 2019; Li et al. 2017; Granados-Muñoz et al., 2012), and the sensitivity of threshold
113 has been discussed across different sites (de Arruda et al., 2018; Manninen et al., 2018; Schween et al., 2014;

114 Barlow et al., 2011; Pearson et al., 2010). A disadvantage of lidar is that it has a large blind range and
115 incapability to penetrate clouds, thus because of that, it is valuable to utilize microwave cloud radar that
116 offers good low altitude coverage and superior performance in cloud penetration. In the cloud observation, a
117 weak echo layer always exists near the surface, from which the vertical velocity can be retrieved. However,
118 there are few reports utilizing vertical velocity obtained from Doppler cloud radar for the CBL
119 investigations.

120 In present study, we estimate the CBLH based on the vertical velocity from a Ka-band millimeter wave
121 cloud radar (MMCR) at Wuhan, and compared this result with that derived from the lidar RCS by three
122 algorithms. Then, the general features of monthly and seasonal mean CBLHs are studied by using the
123 MMCR observation with high temporal resolution. In section 2, the MMCR, lidar and their data are briefly
124 described. In Section 3, we discuss the methods that are used to identify the CBL top from the MMCR and
125 lidar measurements. In section 4, we present four examples of CBLH diurnal evolution in different seasons
126 by comparing the CBL tops retrieved from the MMCR and lidar measurements, and then investigate the
127 monthly and seasonal mean CBLHs over Wuhan in Section 5. Section 6 provides a summary.

128

129 **2. Instruments and Data**

130 In this study, the CBLH derived from the MMCR measurements is compared with that from the lidar
131 measurements. The Ka-band MMCR and lidar are situated at the Atmospheric Remote Sensing Observatory
132 (ARSO) in Wuhan University (30.5°N, 114.4°E). Wuhan, an inland megacity in central China, is located in
133 the east of Jiangnan Plain, with a resident population of over 12 million. The climate of the city is humid,
134 dominated by the subtropical monsoon, which is characterized by abundant precipitation and four distinct
135 seasons (Guo et al., 2023). Due to heavy traffic and industrial activities, large amounts of aerosols are
136 emitted from the industrialized metropolis. Sandstorms from the northwest often pass through Wuhan,

137 especially in spring. These sandstorms cause the remarkable variation in the spatial distribution and
138 concentration of aerosols. Frequent sand and dust activity along with cloudy weather poses significant
139 challenges for the Ka-band MMCR and lidar in accurately capturing the CBL evolution.

140 **2.1 Ka-Band Radar**

141 The WHU-CW MMCR established by the ARSO is a Ka-band frequency-modulated continuous wave
142 (FMCW) Doppler radar, which is shown in Figure 1. The radar system transmits a mean power of 50 W at
143 operating frequency of 35.035 GHz through 0.38° width beam formed by a Cassegrain antenna with 1.5 m
144 diameter. Backscatter echoes from aerosol and cloud particles are received by the other same Cassegrain
145 antenna, and then are sent to the signal processing subsystem to obtain the radial distribution of parameters
146 that represent the characteristics and motion of particles, such as reflectivity factor, Doppler velocity, and
147 Doppler spectrum width. Because of almost continuous transmitting and receiving, FMCW radar has
148 generally a much higher mean power relative to pulse radar, which improves the capacity of MMCR to
149 detect weak echo targets. Meanwhile, by modulating and demodulating the continuous wave, the FMCW
150 radar measurement has an adjustable range and time resolution. In non-precipitation, the MMCR
151 measurement has a temporal resolution of 0.26 s and a maximum unambiguous velocity of 4.30 m s⁻¹, which
152 are adjusted to be 0.104 s and 10.75 m s⁻¹ in precipitation as the size and falling speed of hydrometeors
153 increase (Mao et al., 2023), respectively. The MMCR observation has been applied to the investigations of
154 cloud and precipitation over Wuhan in previous works (Fang et al., 2023; Mao et al., 2023).

155 The MMCR has a maximum detectable distance of about 30 km and a sensitivity of -30 dBZ at the
156 distance of 10 km. In the MMCR measurement, there are weak echoes generally less than -40 dBz within a
157 few kilometers above the surface. The weak echoes near the surface are attributed to the backscattering of
158 small insects and aerial plankton in some studies (Franck et al., 2021; Chandra et al., 2010; Achtemeier,
159 1991), and are also suggested to come from the scattering of dust particles in other studies (Görsdorf et al.,

160 2015; Clothiaux et al, 2000; Moran et al., 1998). Considering that the size of large dust particles, plant
161 aerosol particles, and aerosol particles from combustion can be much larger than 10 μm , it is possible for the
162 large aerosol particles to cause these weak echoes observed by MMCR. The servo-mechanical subsystem
163 conducts the MMCR to work in specified directional mode or scanning mode. In 2020, the MMCR was
164 operated in the vertical pointing mode, and the observation is recorded with a vertical resolution of 30 m. In
165 this study, we attempt to explore the CBL evolution at Wuhan from the Ka-band MMCR observation in
166 2020.

167 **2.2 Polarization Lidar**

168 The WHU-PL polarization lidar developed by ARSO is also located in Wuhan University, about 0.5 km
169 from the Ka-band MMCR. The lidar telescope is 70 m above sea level, which is about 30 m higher than the
170 MMCR antenna. Expanded laser beam overlaps with the full view field of the receiving telescope at a height
171 of 0.3 km, thus this height is the low limit of lidar detection. The lidar data has a temporal resolution of 1
172 min, and the same vertical resolution of 30 m as the MMCR data. In this study, we regard the height of
173 MMCR antenna as a baseline, and then the initial height of lidar data is set at 0.33 km.

174 The lidar system consists of transmitting subsystem receiving subsystem and information processing
175 subsystem. The lidar vertically emits the laser pulses of 120 mJ at operating wavelength of 532 nm with a
176 repetition rate of 20 Hz by a frequency-doubled Nd: YAG laser. The output polarized laser beam has a fine
177 polarization purity with depolarization ratio less than 1:10000 by using a Brewster polarizer. Light
178 backscattered by aerosol and cloud particles and atmospheric molecules is collected by a telescope with 0.3
179 m diameter. After separated through an interference filter with 0.3 nm bandwidth centered at 532 nm, the
180 elastically backscattered light is incident on a polarization beam splitter prism, and then the two-channel
181 polarized light are focused onto two photomultiplier tubes (PMTs), respectively. The signals from the two
182 PMTs are transferred to a personal computer (PC)-controlled two-channel transient digitizer, which can

183 obtain the echo signal intensity and volume depolarization ratio through the PC processing. Backscatter
184 coefficient is retrieved based on the backward iteration algorithm under the condition of a given lidar ratio
185 proposed by Fernald and Klett (Fernald, 1984; Klett, 1981), and then the RCS is derived from the
186 backscatter coefficient (Freudenthaler et al., 2009; Immler and Schrems, 2003). The lidar configuration and
187 depolarization comparison with the measurement from the cloud-aerosol lidar and infrared pathfinder
188 satellite observation (CALIPSO) were in detail described in the early study (Kong and Yi, 2015).

189

190 **3. Methodology**

191 Given that the CBLH is estimated from instruments that retrieve different variables, the algorithms that
192 are utilized to make such estimations are also based on different principles, which are explained in the
193 following subsections.

194 **3.1 Gradient, Variance and Wavelet Transformation Methods**

195 In the lidar observation, the CBLH is derived from the RCS, which is approximately proportional to the
196 aerosol concentration (Kong and Yi, 2015; Lewis et al., 2013; Pal et al., 2010; Emeis et al., 2008). Generally,
197 aerosols are well-mixed within the CBL due to the convectively driven turbulence, and its concentration
198 decays sharply over the CBL top. Hence, the gradient (Grd) method is often utilized to investigate the
199 CBLH by identifying the strongest or minimum gradient of RCS. The wavelet covariance transformation
200 (WCT) method, with a chosen Harr wavelet function, estimates the CBL top by investigating the correlation
201 of the RCS variation with a step function (Zhang et al., 2021; Angelini and Gobbi, 2014; Pal et al., 2010;
202 Baars et al., 2008; Brooks, 2003). Essentially, the WCT method can be considered as a smooth enhancement
203 of Grd method, which may be less affected by noise than the Grd method (Davis et al., 2000; Baars et al. al.,
204 2008).

205 On the other hand, because of the entrainment process, there is a frequent exchange of matter and energy

206 between the CBL and the free atmosphere, causing the dramatic variation of aerosol concentration or lidar
207 RCS on small time scales around the CBL top (Zhang et al., 2018; Kong and Yi, 2015). In this case, the
208 variance (Var) method is used to determine the CBL top by identifying the maximum variance of RCS
209 during a relatively long period (Lammert and Bösenberg, 2006; Martucci et al., 2004; Piironen and Eloranta,
210 1995). We estimate the CBLH from the lidar RCS in a period of 30 min by using the three methods, for
211 instance, the CBLH at 12:00 LT (the same below) is calculated based on the RCS data from 11:45 to 12:15.

212 **3.2 Threshold Method**

213 The variance (σ_w^2) of vertical velocity (w) is representative of the level of turbulent activity, thus a
214 threshold of σ_w^2 is applied to determining the CBLH in the Doppler lidar measurement. The threshold is
215 chosen to be $0.04 \text{ m}^2 \text{ s}^{-2}$ in the regions with weak turbulence (Tucker et al., 2009), $0.3 \text{ m}^2 \text{ s}^{-2}$ in a tropical
216 rainforest (Pearson et al., 2010), and $0.4 \text{ m}^2 \text{ s}^{-2}$ in the regions with central European climate (Schween et al.,
217 2014; Träumner et al., 2011), while the thresholds of 0.1 and $0.2 \text{ m}^2 \text{ s}^{-2}$ are selected in the urban landscapes
218 since the retrieved CBLH is not heavily dependent on the given thresholds (Burgos-Cuevas et al., 2023;
219 Huang et al. 2017; Barlow et al., 2011). Similarly, the threshold method is also used to determine a CBLH
220 from the more than 6000 w profiles in the MMCR measurement during a period of 30 min.

221 Figure 2 presents the distribution of w from the Ka-band MMCR observation and RCS (in arbitrary
222 unit) from the lidar measurement on 15 August 2020. The day is 3 days later than the rainy day of 12 August.
223 By taking observations for a period of 30 min from 11:45 to 12:15, we calculate the mean w and RCS, and
224 estimate the position of CBL top by means of different algorithms, which are shown in Figure 3. From the
225 lidar RCS, the CBLH is 1.35 km in the Grd and WCT methods, and 1.32 km in the Var method. In the
226 MMCR observation, σ_w^2 has a clear downward trend with increasing height, with the values of about 1.36
227 $\text{m}^2 \text{ s}^{-2}$ from the near ground to $0.15 \text{ m}^2 \text{ s}^{-2}$ at 1.47 km, and then maintains slight fluctuations around the value
228 of $0.15 \text{ m}^2 \text{ s}^{-2}$ to higher altitudes. For a specified threshold of $0.3 \text{ m}^2 \text{ s}^{-2}$, the CBL top is identified at the

229 height of 1.35 km, which is in agreement with the lidar results. It can be noted from Figures 3d and 3f that
230 the CBLHs in the mean RCS profile are around the position with the most rapid change, while the CBLH
231 retrieved from the MMCR σ_w^2 is not related to the vertical variation of mean w .

232 As shown in Figure 3e, σ_w^2 decreases quickly from $0.4 \text{ m}^2 \text{ s}^{-2}$ at 1.29 km to $0.15 \text{ m}^2 \text{ s}^{-2}$ at 1.47 km,
233 indicating that the CBH top at noon is less sensitive to the selected threshold within $0.15\text{-}0.4 \text{ m}^2 \text{ s}^{-2}$. Figure 4
234 depicts the CBLHs on 15 August 2020 at the thresholds from 0.2 to $0.45 \text{ m}^2 \text{ s}^{-2}$. Overall, the CBL top
235 declines with the increasing threshold. Nevertheless, the CBLH from 09:30 to 17:30 remains relatively
236 stable with little change at the different thresholds, and the discrepancy among these thresholds arises
237 mainly in the initial growing and final decaying stages of CBL. By comparison (not presented), the CBLH at
238 8:00 derived from the threshold of $\sigma_w^2=0.3 \text{ m}^2 \text{ s}^{-2}$ is generally consistent with the CBLHs estimated by the
239 maximum gradient of potential temperature and a 0.25 threshold of bulk Richardson number based on the
240 radiosonde data at Wuhan, which indicates that the threshold of $\sigma_w^2=0.3 \text{ m}^2 \text{ s}^{-2}$ is appropriate for the CBLH
241 estimation at Wuhan. In following analysis, we take $0.3 \text{ m}^2 \text{ s}^{-2}$ as the threshold to determine the CBLH in the
242 MMCR observation.

243

244 4. Case Investigation and Comparison

245 Figure 5 presents the CBLH evolution on 15 August 2020 from the lidar RCS based on the Grd, Var and
246 WCT methods, and the comparison with that obtained from the MMCR σ_w^2 , together with the distribution
247 of MMCR reflectivity factor in the range of 10-15 km. As shown in Figure 5c, due to the influence of
248 aerosol residual layer, the CBLH from the lidar RCS fluctuates from about 1.56 km at 06:00 down to 1.17
249 km at 09:30, however, with the sunrise at 05:50, the CBL top derived from the MMCR σ_w^2 gradually rises
250 from about 0.09 km at 06:00 to 1.17 km at 09:30. It is interesting that the CBLH from the lidar RCS
251 variance drops at 07:30 and then shows a change similar to that from the MMCR σ_w^2 . Both the variances of

252 w and RCS represent the deviation degree of their small time scale values relative to their 30 min-mean
253 values, which may be responsible for the similar results. When the CBL ascends gradually and mixes with
254 the residual layer, the CBLHs in the lidar and MMCR observations are consistent with each other between
255 09:30 and 17:00, including a slight drop at 12:30 and 14:30 (from the gradient and variance of RCS). The
256 maximum height of CBL is about 1.71 km at 14:00 and 15:00 based on σ_w^2 and the RCS gradient and
257 variance.

258 One can note from the reflectivity factor distribution in Figure 5b that cirrus clouds occur from 17:00,
259 develop rapidly into the thick clouds at about 11-14.4 km at 17:30, and then dissipate quickly after 17:30. In
260 the MMCR observation, the CBLH shows a clear dip between 17:30 and 18:30, and then a lift as the clouds
261 dissipates rapidly. Earlier studies from the Doppler lidar w investigated the complex influence of low-level
262 clouds on the CBL and turbulence. The cloud-top radiative cooling drives top-down convective mixing,
263 leading to the enhancement of σ_w^2 (Hogan et al., 2009; Harvey et al., 2013; Manninen et al., 2018).
264 Whereas, during the warm season, the magnitude of σ_w^2 from the lidar w is large on clear-sky days and
265 decreases on cloud-topped days, and the intensity of turbulence reduces with an increase in the cloud
266 fraction within the CBL, except in the cloud layer that exceeds 90% of the CBL thickness (Dewani et al.,
267 2023). Here, the cirrus clouds are above 11 km, thus the cloud-top driven convective mixing has little impact
268 on the low atmosphere, however, the thick clouds cool the surface by attenuating solar radiation, which can
269 weaken the surface-driven convective mixing. Therefore, the thick cirrus makes a large contribution to the
270 CBLH dip. The phenomenon of CBLH dip also arises in the lidar RCS, especially from the RCS variance,
271 but with a time lag due to the influence of a long time-mixing process on the aerosol distribution
272 (Burgos-Cuevas et al., 2023; Schween et al., 2014). After the sunset at 19:05, the CBLH retrieved by σ_w^2
273 drops quickly to 0.27 km at 20:00 from 1.47 km at 19:00, while the top of aerosol residual layer (or
274 horizontally migrating aerosol layer) identified by the lidar stays at a far higher level, especially from the

275 RCS gradient and WCT.

276 Next, we select the observations on 31 January, 12 November, and 19 March 2020 to compare the CBLH
277 evolutions. The three days, without clouds and precipitation, are chosen as the representative in different
278 seasons. Figure 6 shows the CBLHs on 31 January derived from the four methods above, which are overlaid
279 on the MMCR w and σ_w^2 and the lidar RCS, respectively. January is the coldest month of the year, and
280 on 31 January, the minimum (maximum) temperature is -5 °C (4 °C) recorded in the weather forecast.
281 Owing to the convection inhibited largely by the frigid surface and air, σ_w^2 shows that the CBLH develops
282 very slowly upward to 0.3 km at 11:30 from 0.12 km at 07:30 as the sun rises at 07:15. Thereafter, the top of
283 CBL escalates quickly to 0.9 km at 13:30, and reaches the maximum height of 0.99 km at 14:30, and during
284 this period, the CBLH from the lidar RCS experiences a similarly rapid uplift, and attains the peak of 1.2 km
285 at 14:00 from the RCS gradient and variance, and 1.14 km at 14:30 from the RCS WCT. In addition, it can
286 be seen from Figure 6d that all the CBLHs from the lidar RCS are slightly larger than those from the
287 MMCR σ_w^2 , which may be attributed to the long time-mixing aerosols and wet surface in winter. After
288 14:30, the CBLH from σ_w^2 descends gradually, and approaches the ground at 17:30 prior to the sunset at
289 17:57, while at the sunset, the CBL top from the RCS is at 0.8-0.9 km due to the long time-mixing
290 processes.

291 Figure 7 presents the CBLHs determined from the MMCR and lidar observations on 12 November 2020.
292 With the sunset on this day in late autumn, the CBLH identified from σ_w^2 displays a little fluctuation until
293 10:30. After then, the CBL is rapidly developed to 0.51 km at 11:30, and mixes fully with the residual layer
294 retrieved from the lidar RCS, thus the CBL tops have approximately the same evolution between the MMCR
295 and lidar observations from 11:30 to 17:30, with the maximum values of about 0.75-0.78 km at 15:00 and
296 16:00. As the sun goes down at 17:27, the CBL from σ_w^2 rapidly shrinks close to the ground at 18:00, and
297 aerosol particles left in the air form a residual layer, similar to the two cases above.

298 Figure 8 depicts the CBLH variations in the MMCR and lidar observations on 19 March 2020, together
299 with the depolarization ratio from the lidar. In spring, sand and dust with different intensities from the
300 northwest of China pass frequently through Wuhan. On this day, there is a fine sand and dust layer mostly
301 above 1.8 km, with the depolarization ratios of about 0.08-0.12 in Figure 8c, which can also be noted from
302 the distribution of w in the MMCR observation. Meanwhile, another sand and dust layer with the larger
303 depolarization ratios of about 0.14-0.16 passes through Wuhan from about 14:00, and mixes with the lower
304 part of the first sand and dust layer. In this situation, the MMCR observation indicates that the CBL starts to
305 develop gently upward from the sunrise, and the upward trend of CBLH is also presented in the lidar
306 measurement, but at higher altitudes. At 09:30, the CBLH is about 0.48 km in both the MMCR and lidar
307 observations, and then rises steadily to 1.32 km at 16:00 and 16:30, showing a good agreement between the
308 two observations. Subsequently, the CBLH from σ_w^2 undergoes two rapid declines. One occurs from 1.2
309 km at 17:00 to 0.51 km at 18:00, which is probably related to the sand and dust deposition in addition to the
310 diminished radiation in the late afternoon, and the other arises after the sunset. However, because of the
311 effect of sand and dust, the CBLH from the lidar RCS increases slightly from 1.32 km at 16:30 to about 1.38
312 km at 18:00 and 18:30, and then decreases gradually with time.

313 The CBLH is identified by the spatial and temporal variation of aerosol concentration from the lidar
314 measurement and by the temporal change of w from the MMCR observation. The four examples
315 demonstrate that except for the periods with the influence of aerosol residual layer, particularly during the
316 few hours after sunrise and before sunset, the MMCR CBLHs are generally in agreement with the lidar
317 CBLHs. The residual layer causes a higher CBLH estimated by the lidar RCS than by the MMCR w
318 because σ_w^2 is less contaminated by the residual layer relative to the aerosol concentration. Additionally,
319 the CBLH estimated by σ_w^2 shows a rapid response to thick high-level clouds and less influence by the
320 long-range transport of sand and dust. Hence, the MMCR observation can accurately retrieve the CBLH and

321 capture its diurnal evolution, especially for the CBL in the blind range of lidar.

322

323 **5. Monthly and Seasonal Mean CBLHs**

324 To reveal the general characteristics of CBLH diurnal evolution in different months and seasons, we
325 calculate the monthly and seasonal mean CBLHs by using the MMCR w on these days without
326 precipitation in 2020. We consider that winter covers the months of December, January and February, while
327 March, April and May are spring, June, July and August are summer and the rest is autumn.

328 Figure 9 illustrates the averaged CBLHs with the standard deviations superimposed on the mean σ_w^2 in
329 each month and season. As the spot of direct sunlight slowly moves northward, the mean variance gradually
330 increases from January to July, and then decreases gradually from August to December, moreover, the
331 coverage height and time duration of its large values show an analogous monthly variation. In this case, the
332 peak height of CBL ascends steadily from 0.66 km in January to 1.47 (1.44) km in July (August), and
333 subsequently, descends gradually to the lowest height of 0.42 km in December. Additionally, at Wuhan, the
334 plum rain starts in June and prevails in July. As shown in Figure 9, the CBLH in July has the largest standard
335 deviation (between 13:00 and 19:00), which is possibly attributable to the cloudy and rainy weather besides
336 the strongest radiation.

337 As for seasonal variation, as we expected, the mean σ_w^2 is the strongest in summer and the weakest in
338 winter. Interestingly, the variance is significantly larger in spring than in autumn. Not only the maximum
339 CBLH of 1.14 km at 13:30 in spring is much higher than that of about 0.66 km at 13:30 and 14:00 in autumn,
340 but also the mean σ_w^2 of $0.42 \text{ m}^2 \text{ s}^{-2}$ in the CBL during spring is stronger than that of $0.35 \text{ m}^2 \text{ s}^{-2}$ during
341 autumn. The maximum height of CBL is 1.29 km at 14:30 and 15:00 in summer, and about 0.6 km at 14:30
342 in winter. In summer, the CBLH displays a feature of quick descent near twilight, and in autumn, the CBL
343 shows a wider envelope with an earlier development and a later dissipation relative to that in winter though

344 their maximum CBLHs are almost the same. In previous studies, based on the threshold of σ_w^2 from the
345 Doppler lidar measurement in Mexico City (19.3° N, 99.1° E), the CBLH is higher in spring and summer,
346 and lower in winter, while the maximum CBLH of about 1.5 km occurs in May, which is because the CBLH
347 is suppressed to some extent by increased cloud cover in the rainy season between June and September
348 (Burgos-Cuevas et al., 2021). However, the CBLH retrieved from the ceilometer backscatter data is
349 obviously larger than that from the threshold of σ_w^2 (Burgos-Cuevas et al., 2021; Tang et al., 2016).
350 Similarly, in the estimation of CBLH from the lidar RCS over Wuhan and Granada (37.18° N, 3.60° E), the
351 maximum values of seasonal mean CBLHs in all the seasons are larger than those in our results although the
352 gradual ascent of CBLH from winter and autumn to spring and summer is consistent with that in our results
353 (Kong and Yi, 2015; Granados-Muñoz et al., 2012).

354

355 **6. Summary**

356 In this study, we estimate the CBLH from the profile of w in the Ka-MMCR observation by using a
357 threshold of σ_w^2 , which is compared with that from the RCS in the lidar measurement by utilizing the
358 gradient, variance and wavelet methods. Then, we investigate the diurnal evolution of monthly and seasonal
359 mean CBLHs based on the MMCR observation.

360 Although the RCS is proportional to aerosol concentration and w represents the vertical motion of
361 aerosol particles, the comparison of four examples in different seasons indicates that the CBLHs from the
362 MMCR w are in good agreement with those from the lidar RCS, except for the initial growth and final
363 decay phases. The discrepancy can mainly be attributed to the aerosol residual layer and the lidar blind
364 range. The influence of residual layer on the lidar RCS generally causes an overestimation of CBLH,
365 meanwhile, it is impossible for lidar to capture the CBL top within its large blind range. In addition, the
366 CBLH in the MMCR observation shows less contamination by the long-range transport of sand and dust,

367 and thick high-level clouds due to the rapid response of aerosol w relative to its concentration. In this case,
368 the MMCR observation can capture the diurnal evolution of CBLH.

369 Using the profile of w from the MMCR observation on these days without precipitation in 2020, we
370 investigate the diurnal evolution of monthly and seasonal mean CBLHs. The maximum value of monthly
371 mean CBLH increases gradually from 0.66 km in January to 1.47 (1.44) km in July (August), and then
372 decreases to the lowest height of 0.42 km in December. As for the seasonal behavior, the mean CBLH has
373 the maximum heights of 1.29 km at 14:30 and 15:00 in summer, 1.14 km at 13:30 in spring, 0.66 km at
374 13:30 and 14:00 in autumn, and 0.6 km at 14:30 in winter. In addition, the statistical standard deviations are
375 monthly-dependent, indicating that the CBLH is not only mainly regulated by the surface heating associated
376 with solar radiation, but also significantly affected by weather conditions, such as humidity and clouds.
377 Therefore, since the Ka-band MMCR is a powerful instrument for observing clouds and weak precipitation,
378 the full-time MMCR observation with low blind height can obtain the entire diurnal evolution of CBLH,
379 which helps us gain an insight into CBL features and also provides important input variables for weather
380 prediction and climate models.

381

382

383 **Code availability.** Software code to obtain the results is available upon request from the corresponding
384 author.

385 **Data availability.** All data used are available upon request from the corresponding author.

386 **Author contributions.** KH and FY conceptualized this study. ZZ and KH completed the analysis and the
387 manuscript. FL, JZ, YJ, and FY discussed the results and finalized the manuscript.

388 **Competing interests.** The authors declare that they have no conflict of interest.

389 **Financial support.** This work was supported by the National Key Research and Development Program of

390 China (2022YFB3901800 and 2022YFF0503700) and the National Natural Science Foundation of China
391 (42174189).

392

393

394 **References**

395 Allabakash, S., Yasodha, P., Bianco, L., Venkatramana Reddy, S., Srinivasulu, P., and Lim, S.: Improved
396 boundary layer height measurement using a fuzzy logic method: Diurnal and seasonal variabilities of
397 the convective boundary layer over a tropical station, *J. Geophys. Res.-Atmos.*, 122, 9211–9232,
398 <https://doi.org/10.1002/2017JD027615>, 2017.

399 Achtemeier, G. L.: The use of insects as tracers for “Clear-Air” boundary-layer studies by doppler radar, *J.*
400 *Atmos. Ocean. Tech.*, 8, 746-765,
401 [https://doi.org/10.1175/1520-0426\(1991\)008<0746:TUOIAT>2.0.CO;2](https://doi.org/10.1175/1520-0426(1991)008<0746:TUOIAT>2.0.CO;2), 1991.

402 Baars, H., Ansmann, A., Engelmann, R., and Althausen, D.: Continuous monitoring of the boundary-layer
403 top with lidar, *Atmos. Chem. Phys.*, <https://doi.org/10.5194/acp-8-7281-2008>, 2008.

404 Barlow, J. F., Dunbar, T. M., Nemitz, E. G., Wood, C. R., Gallagher, M. W., Davies, F., O’Connor, E., and
405 Harrison, R. M.: Boundary layer dynamics over London, UK, as observed using Doppler lidar during
406 REPARTEE-II, *Atmos. Chem. Phys.*, 11, 2111–2125, <https://doi.org/10.5194/acp-11-2111-2011>, 2011.

407 Basha, G. and Ratnam, M. V.: Identification of atmospheric boundary layer height over a tropical station
408 using high-resolution radiosonde refractivity profiles: Comparison with GPS radio occultation
409 measurements, *J. Geophys. Res.-Atmos.*, 114, 2008JD011692, <https://doi.org/10.1029/2008JD011692>,
410 2009.

411 Bernardini, M., Pirozzoli, S., and Orlandi, P.: Compressibility effects on roughness-induced boundary layer
412 transition, *Int. J. Heat Fluid Fl.*, 35, 45–51, <https://doi.org/10.1016/j.ijheatfluidflow.2012.02.007>, 2012.

413 Bianco, L. and Wilczak, J. M.: Convective boundary layer depth: Improved measurement by doppler radar
414 wind profiler using fuzzy logic methods, *J. Atmos. Ocean. Tech.*, 19, 1745–1758,
415 [https://doi.org/10.1175/1520-0426\(2002\)019<1745:CBLDIM>2.0.CO;2](https://doi.org/10.1175/1520-0426(2002)019<1745:CBLDIM>2.0.CO;2), 2002.

416 Bianco, L., Muradyan, P., Djalalova, I., Wilczak, J. M., Olson, J. B., Kenyon, J. S., Kotamarthi, R., Lantz, K.,
417 Long, C. N., and Turner, D. D.: Comparison of observations and predictions of daytime
418 planetary-boundary-layer heights and surface meteorological variables in the Columbia river gorge and
419 basin during the second wind forecast improvement project, *Bound.-Lay. Meteorol.*, 182, 147–172,
420 <https://doi.org/10.1007/s10546-021-00645-x>, 2022.

421 Blay-Carreras, E., Pino, D., Vilà-Guerau De Arellano, J., Van De Boer, A., De Coster, O., Darbieu, C.,
422 Hartogensis, O., Lohou, F., Lothon, M., and Pietersen, H.: Role of the residual layer and large-scale
423 subsidence on the development and evolution of the convective boundary layer, *Atmos. Chem. Phys.*,
424 14, 4515–4530, <https://doi.org/10.5194/acp-14-4515-2014>, 2014.

425 Brooks, I. M.: Finding Boundary Layer Top: Application of a wavelet covariance transform to lidar
426 backscatter profiles, *J. Atmos. Ocean. Tech.*, 20, 1092–1105,
427 [https://doi.org/10.1175/1520-0426\(2003\)020<1092:FBLTAO>2.0.CO;2](https://doi.org/10.1175/1520-0426(2003)020<1092:FBLTAO>2.0.CO;2), 2003.

428 Brooks, I. M. and Fowler, A. M.: A new measure of entrainment zone structure, *Geophys. Res. Lett.*, 34,
429 2007GL030958, <https://doi.org/10.1029/2007GL030958>, 2007.

430 Burgos-Cuevas, A., Adams, D. K., García-Franco, J.L., and Ruiz-Angulo, A.: A seasonal climatology of the
431 Mexico City atmospheric boundary layer, *Bound.-Lay. Meteorol.*, 180, 131–154,
432 <https://doi.org/10.1007/s10546-021-00615-3>, 2021.

433 Burgos-Cuevas, A., Magaldi, A., Adams, D. K., Grutter, M., García-Franco, J. L., and Ruiz-Angulo, A.:
434 Boundary layer height characteristics in Mexico City from two remote sensing techniques, *Bound.-Lay.*
435 *Meteorol.*, 186, 287–304, <https://doi.org/10.1007/s10546-022-00759-w>, 2023.

436 Chandra, A. S., Kollias, P., Giangrande, S. E., and Klein, S. A.: Long-term observations of the convective
437 boundary layer using insect radar returns at the SGP ARM climate research facility, *J. Climate*, 23,
438 5699–5714, <https://doi.org/10.1175/2010JCLI3395.1>, 2010.

439 Clothiaux, E. E., Ackerman, T. P., Mace, G. G., Moran, K. P., Marchand, R. T., Miller, M. A., and Martner, B.
440 E.: Objective determination of cloud heights and radar reflectivities using a combination of active
441 remote sensors at the ARM CART sites, *J. Appl. Meteorol.*, 39, 645–665,
442 [https://doi.org/10.1175/1520-0450\(2000\)039<0645:ODOCHA>2.0.CO;2](https://doi.org/10.1175/1520-0450(2000)039<0645:ODOCHA>2.0.CO;2), 2000.

443 Dang, R., Yang, Y., Hu, X.-M., Wang, Z., and Zhang, S.: A review of techniques for diagnosing the
444 atmospheric boundary layer height (ABLH) using aerosol lidar data, *Remote Sens.-Basel*, 11, 1590,
445 <https://doi.org/10.3390/rs11131590>, 2019.

446 Davis, K. J., N. Gamage, C. Hagelberg, C. Kiemle, D. Lenschow, and P. Sullivan: An objective method for
447 deriving atmospheric structure from airborne lidar observations, *J. Atmos. Ocean. Tech.*, 17,
448 1455–1468, doi:10.1175/1520-0426(2000)017<1455:AOMFDA>2.0.CO;2, 2000.

449 de Arruda Moreira, G., Guerrero-Rascado, J. L., Bravo-Aranda, J. A., Benavent-Oltra, J. A., Ortiz-Amezcu,
450 P., Román, R., Bedoya-Velásquez, A. E., Landulfo, E., and Alados-Arboledas, L.: Study of the
451 planetary boundary layer by microwave radiometer, elastic lidar and Doppler lidar estimations in
452 Southern Iberian Peninsula, *Atmos. Res.*, 213, 185–195, <https://doi.org/10.1016/j.atmosres.2018.06.007>,
453 2018.

454 Dewani, N., Sakradzija, M., Schlemmer, L., Leinweber, R., and Schmidli, J.: Dependency of vertical
455 velocity variance on meteorological conditions in the convective boundary layer, *Atmos. Chem. Phys.*,
456 23, 4045–4058, <https://doi.org/10.5194/acp-23-4045-2023>, 2023.

457 Edwards, J. M., Beljaars, A. C. M., Holtslag, A. A. M., and Lock, A. P.: Representation of boundary-layer
458 processes in numerical weather prediction and climate models, *Bound.-Lay. Meteorol.*, 177, 511–539,

459 <https://doi.org/10.1007/s10546-020-00530-z>, 2020.

460 Emeis, S., K. Schäfer, and C. Münkler: Surface-based remote sensing of the mixing-layer height—A review,
461 *Meteorol. Z.*, 17, 621–630, <https://doi.org/10.1127/0941-2948/2008/0312>, 2008.

462 Fang, J., Huang, K., Du, M., Zhang, Z., Cao, R., and Yi, F.: Investigation on cloud vertical structures based
463 on Ka-band cloud radar observations at Wuhan in Central China, *Atmos. Res.*, 281, 106492,
464 <https://doi.org/10.1016/j.atmosres.2022.106492>, 2023.

465 Fernald, F. G.: Analysis of atmospheric lidar observations: Some comments, *Appl. Opt.*, 23, 652–653,
466 <https://doi.org/10.1364/AO.23.000652>, 1984.

467 Franck, A., Moisseev, D., Vakkari, V., Leskinen, M., Lampilahti, J., Kerminen, V.-M., and O’Connor, E.:
468 Evaluation of convective boundary layer height estimates using radars operating at different frequency
469 bands, *Atmos. Meas. Tech.*, 14, 7341–7353, <https://doi.org/10.5194/amt-14-7341-2021>, 2021.

470 Freudenthaler, V., Esselborn, M., Wiegner, M., Heese, B., Tesche, M., Ansmann, A., Müller, D., Althausen,
471 D., Wirth, M., Fix, A., Ehret, G., Knippertz, P., Toledano, C., Gasteiger, J., Garhammer, M., and
472 Seefeldner, M.: Depolarization ratio profiling at several wavelengths in pure Saharan dust during
473 SAMUM 2006, *Tellus B*, 61, 165, <https://doi.org/10.1111/j.1600-0889.2008.00396.x>, 2009.

474 Görndorf, U., Lehmann, V., Bauer-Pfundstein, M., Peters, G., Vavriv, D., Vinogradov, V., and Volkov, V.: A
475 35-GHz polarimetric doppler radar for long-term observations of cloud parameters—description of
476 system and data processing, *J. Atmos. Ocean. Tech.*, 32, 675–690,
477 <https://doi.org/10.1175/JTECH-D-14-00066.1>, 2015.

478 Granados-Muñoz, M. J., Navas-Guzmán, F., Bravo-Aranda, J. A., Guerrero-Rascado, J. L., Lyamani, H.,
479 Fernández-Gálvez, J., and Alados-Arboledas, L.: Automatic determination of the planetary boundary
480 layer height using lidar: One-year analysis over southeastern Spain, *J. Geophys. Res.-Atmos.*, 117,
481 <https://doi.org/10.1029/2012JD017524>, 2012.

482 Grossman and Robert, L.: Observed effects of horizontal radiative surface temperature variations on the
483 atmosphere over a midwest watershed during CASES 97, *J. Geophys. Res.-Atmos.*, 110,
484 <https://doi.org/10.1029/2004JD004542>, 2005.

485 Guo, J., Miao, Y., Zhang, Y., Liu, H., Li, Z., Zhang, W., He, J., Lou, M., Yan, Y., Bian, L., and Zhai, P.: The
486 climatology of planetary boundary layer height in China derived from radiosonde and reanalysis data,
487 *Atmos. Chem. Phys.*, 16, 13309–13319, <https://doi.org/10.5194/acp-16-13309-2016>, 2016.

488 Guo, J., Su, T., Li, Z., Miao, Y., Li, J., Liu, H., Xu, H., Cribb, M., and Zhai, P.: Declining frequency of
489 summertime local-scale precipitation over eastern China from 1970 to 2010 and its potential link to
490 aerosols, *Geophys. Res. Lett.*, 44, 5700–5708, <https://doi.org/10.1002/2017GL073533>, 2017.

491 Guo, J., Zhang, J., Yang, K., Liao, H., Zhang, S., Huang, K., Lv, Y., Shao, J., Yu, T., Tong, B., Li, J., Su, T.,
492 Yim, S. H. L., Stoffelen, A., Zhai, P., and Xu, X.: Investigation of near-global daytime boundary layer
493 height using high-resolution radiosondes: first results and comparison with ERA5, MERRA-2, JRA-55,
494 and NCEP-2 reanalyses, *Atmos. Chem. Phys.*, 21, 17079–17097,
495 <https://doi.org/10.5194/acp-21-17079-2021>, 2021.

496 Guo, X., Huang, K., Fang, J., Zhang, Z., Cao, R., Yi, F.: Seasonal and diurnal changes of air temperature and
497 water vapor observed with a microwave radiometer in Wuhan, China, *Remote Sens.-Basel*, 15, 5422.
498 <https://doi.org/10.3390/rs15225422>, 2023.

499 Heus, T., Van Heerwaarden, C. C., Jonker, H. J. J., Pier Siebesma, A., Axelsen, S., Van Den Dries, K.,
500 Geoffroy, O., Moene, A. F., Pino, D., De Roode, S. R., and Vilà-Guerau De Arellano, J.: Formulation of
501 the Dutch Atmospheric Large-Eddy Simulation (DALES) and overview of its applications, *Geosci.*
502 *Model Dev.*, 3, 415–444, <https://doi.org/10.5194/gmd-3-415-2010>, 2010.

503 Holtslag, A. A. M. and Nieuwstadt, F. T. M.: Scaling the atmospheric boundary layer, *Bound.-Lay. Meteorol.*,
504 36, 201–209, <https://doi.org/10.1007/BF00117468>, 1986.

505 Huang, M., Gao, Z., Miao, S., Chen, F., LeMone, M. A., Li, J., Hu, F., and Wang, L.: Estimate of
506 boundary-layer depth over Beijing, China, using doppler lidar data during SURF-2015, *Bound.-Lay.*
507 *Meteorol.*, 162, 503–522, <https://doi.org/10.1007/s10546-016-0205-2>, 2017.

508 Immler, F. and Schrems, O.: Vertical profiles, optical and microphysical properties of Saharan dust layers
509 determined by a ship-borne lidar, *Atmos. Chem. Phys.*, <https://doi.org/10.5194/acp-3-1353-2003>, 2003.

510 Klett, J. D.: Stable analytical inversion solution for processing lidar returns, *Appl. Opt.*, 20, 211–220,
511 <https://doi.org/10.1364/AO.20.000211>, 1981.

512 Kong, W. and Yi, F.: Convective boundary layer evolution from lidar backscatter and its relationship with
513 surface aerosol concentration at a location of a central China megacity, *J. Geophys. Res.-Atmos.*, 120,
514 7928–7940, <https://doi.org/10.1002/2015JD023248>, 2015.

515 Kwon, H.-G., Yang, H., and Yi, C.: Study on radiative flux of road resolution during winter based on local
516 weather and topography, *Remote Sens.-Basel*, 14, 6379, <https://doi.org/10.3390/rs14246379>, 2022.

517 Lammert, A. and Bösenberg, J.: Determination of the convective boundary-layer height with laser remote
518 sensing, *Bound.-Lay. Meteorol.*, 119, 159–170, <https://doi.org/10.1007/s10546-005-9020-x>, 2006.

519 LeMone, M. A., Chen, F., Tewari, M., Dudhia, J., Geerts, B., Miao, Q., Coulter, R. L., and Grossman, R. L.:
520 Simulating the IHOP_2002 fair-weather CBL with the WRF-ARW–Noah modeling system. Part I:
521 Surface fluxes and CBL structure and evolution along the eastern track, *Mon. Weather Rev.*, 138,
522 722–744, <https://doi.org/10.1175/2009MWR3003.1>, 2010.

523 Lewis, J., E. J. Welton, A. M. Molod, and E. Joseph: Improved boundary layer depth retrievals from
524 MPLNET, *J. Geophys. Res.-Atmos.*, 118, 9870–9879, <https://doi.org/10.1002/jgrd.50570>, 2013.

525 Li, H., Yang, Y., Hu, X., Huang, Z., Wang, G., Zhang, B., and Zhang, T.: Evaluation of retrieval methods of
526 daytime convective boundary layer height based on lidar data, *J. Geophys. Res.-Atmos.*, 122,
527 4578–4593, <https://doi.org/10.1002/2016JD025620>, 2017.

528 Liu, B., Guo, J., Gong, W., Shi, L., Zhang, Y., and Ma, Y.: Characteristics and performance of wind profiles
529 as observed by the radar wind profiler network of China, *Atmos. Meas. Tech.*, 13, 4589–4600,
530 <https://doi.org/10.5194/amt-13-4589-2020>, 2020.

531 Liu, F., Yi, F., Yin, Z., Zhang, Y., He, Y., and Yi, Y.: Measurement report: characteristics of clear-day
532 convective boundary layer and associated entrainment zone as observed by a ground-based polarization
533 lidar over Wuhan (30.5° N, 114.4° E), *Atmos. Chem. Phys.*, 21, 2981–2998,
534 <https://doi.org/10.5194/acp-21-2981-2021>, 2021.

535 Liu, S. and Liang, X.-Z.: Observed diurnal cycle climatology of planetary boundary layer height, *J. Climate*,
536 23, 5790–5809, <https://doi.org/10.1175/2010JCLI3552.1>, 2010.

537 Mahrt, L.: Stratified atmospheric boundary layers, *Bound.-Lay. Meteorol.*, 90, 375–396,
538 <https://doi.org/10.1023/A:1001765727956>, 1999.

539 Manninen, A. J., Marke, T., Tuononen, M., and O’Connor, E. J.: Atmospheric boundary layer classification
540 with doppler lidar, *J. Geophys. Res.-Atmos.*, 123, 8172–8189, <https://doi.org/10.1029/2017JD028169>,
541 2018.

542 Mao, Z., Huang, K., Fang, J., Zhang, Z., Cao, R., and Yi, F.: An Observation of precipitation during cooling
543 with Ka-Band cloud radar in Wuhan, China, *Remote Sens.-Basel*, 15, 5397,
544 <https://doi.org/10.3390/rs15225397>, 2023.

545 Martucci, G., R. Matthey, V. Mitev, and H. Richner: Comparison between backscatter lidar and radiosonde
546 measurements of the diurnal and nocturnal stratification in the lower troposphere, *J. Atmos. Ocean.*
547 *Tech.*, 24, 1231–1244, <https://doi.org/10.1175/JTECH2036.1>, 2007.

548 Moran, K. P., Martner, B. E., Post, M. J., Kropfli, R. A., Welsh, D. C., and Widener, K. B.: An unattended
549 cloud-profiling radar for use in climate research, *B. Am. Meteorol. Soc.*, 79, 443–455,
550 [https://doi.org/10.1175/1520-0477\(1998\)079<0443:AUCPRF>2.0.CO;2](https://doi.org/10.1175/1520-0477(1998)079<0443:AUCPRF>2.0.CO;2), 1998.

551 Neggers, R. A. J., Siebesma, A. P., Lenderink, G., and Holtslag, A. A. M.: An evaluation of mass flux
552 closures for diurnal cycles of shallow cumulus, *Mon. Weather Rev.*, 132, 2525–2538,
553 <https://doi.org/10.1175/MWR2776.1>, 2004.

554 Pal, S., Behrendt, A., and Wulfmeyer, V.: Elastic-backscatter-lidar-based characterization of the convective
555 boundary layer and investigation of related statistics, *Ann. Geophys.-Italy*, 28, 825–847,
556 <https://doi.org/10.5194/angeo-28-825-2010>, 2010.

557 Pal, S., Lopez, M., Schmidt, M., Ramonet, M., Gibert, F., Xueref-Remy, I., and Ciais, P.: Investigation of the
558 atmospheric boundary layer depth variability and its impact on the 222 Rn concentration at a rural site
559 in France, *J. Geophys. Res.-Atmos.*, 120, 623–643, <https://doi.org/10.1002/2014JD022322>, 2015.

560 Pearson, G., Davies, F., and Collier, C.: Remote sensing of the tropical rain forest boundary layer using
561 pulsed Doppler lidar, *Atmos. Chem. Phys.*, 10, 5891–5901, <https://doi.org/10.5194/acp-10-5891-2010>,
562 2010.

563 Piironen, A. K. and Eloranta, E. W.: Convective boundary layer mean depths and cloud geometrical
564 properties obtained from volume imaging lidar data, *J. Geophys. Res.-Atmos.*, 100, 25569–25576,
565 <https://doi.org/10.1029/94JD02604>, 1995.

566 Ribeiro, F. N. D., Oliveira, A. P. D., Soares, J., Miranda, R. M. D., Barlage, M., and Chen, F.: Effect of sea
567 breeze propagation on the urban boundary layer of the metropolitan region of Sao Paulo, Brazil, *Atmos.*
568 *Res.*, 214, 174–188, <https://doi.org/10.1016/j.atmosres.2018.07.015>, 2018.

569 Sandeep, A., Rao, T. N., Ramkiran, C. N., and Rao, S. V. B.: Differences in atmospheric boundary-layer
570 characteristics between wet and dry episodes of the Indian summer monsoon, *Bound.-Lay. Meteorol.*,
571 153, 217–236, <https://doi.org/10.1007/s10546-014-9945-z>, 2014.

572 Schneider, S. P.: Effects of roughness on hypersonic boundary-layer transition, *J. Spacecraft Rockets*, 45,
573 193–209, <https://doi.org/10.2514/1.29713>, 2008.

574 Schween, J. H., Hirsikko, A., Löhnert, U., and Crewell, S.: Mixing-layer height retrieval with ceilometer and
575 Doppler lidar: from case studies to long-term assessment, *Atmos. Meas. Tech.*, 7, 3685–3704,
576 <https://doi.org/10.5194/amt-7-3685-2014>, 2014.

577 Seibert, P.: Review and intercomparison of operational methods for the determination of the mixing height,
578 *Atmos. Environ.*, 34, 1001–1027, [https://doi.org/10.1016/S1352-2310\(99\)00349-0](https://doi.org/10.1016/S1352-2310(99)00349-0), 2000.

579 Seidel, D. J., Ao, C. O., and Li, K.: Estimating climatological planetary boundary layer heights from
580 radiosonde observations: Comparison of methods and uncertainty analysis, *J. Geophys. Res.-Atmos.*,
581 115, 2009JD013680, <https://doi.org/10.1029/2009JD013680>, 2010.

582 Seidel, D. J., Zhang, Y., Beljaars, A., Golaz, J., Jacobson, A. R., and Medeiros, B.: Climatology of the
583 planetary boundary layer over the continental United States and Europe, *J. Geophys. Res.-Atmos.*, 117,
584 2012JD018143, <https://doi.org/10.1029/2012JD018143>, 2012.

585 Singh, N., Solanki, R., Ojha, N., Janssen, R. H. H., Pozzer, A., and Dhaka, S. K.: Boundary layer evolution
586 over the central Himalayas from radio wind profiler and model simulations, *Atmos. Chem. Phys.*, 16,
587 10559–10572, <https://doi.org/10.5194/acp-16-10559-2016>, 2016.

588 Solanki, R., Guo, J., Li, J., Singh, N., Guo, X., Han, Y., Lv, Y., Zhang, J., and Liu, B.:
589 Atmospheric-boundary-layer-height variation over mountainous and urban sites in Beijing as derived
590 from radar wind-profiler measurements, *Bound.-Lay. Meteorol.*, 181, 125–144,
591 <https://doi.org/10.1007/s10546-021-00639-9>, 2021.

592 Stull, R. B.: *An Introduction to Boundary Layer Meteorology*, Springer Netherlands, Dordrecht,
593 <https://doi.org/10.1007/978-94-009-3027-8>, 1988.

594 Su, T., Li, Z., and Kahn, R.: A new method to retrieve the diurnal variability of planetary boundary layer
595 height from lidar under different thermodynamic stability conditions, *Remote Sens.-Basel Environ.*,
596 237, 111519, <https://doi.org/10.1016/j.rse.2019.111519>, 2020.

597 Tang, G., Zhang, J., Zhu, X., Song, T., Münkel, C., Hu, B., Schäfer, K., Liu, Z., Zhang, J., Wang, L., Xin, J.,
598 Suppan, P., and Wang, Y.: Mixing layer height and its implications for air pollution over Beijing, China,
599 *Atmos. Chem. Phys.*, 16, 2459–2475, <https://doi.org/10.5194/acp-16-2459-2016>, 2016.

600 Tennekes, H. and Driedonks, A. G. M.: Basic entrainment equations for the atmospheric boundary layer,
601 *Bound.-Lay. Meteorol.*, 20, 515–531, <https://doi.org/10.1007/BF00122299>, 1981.

602 Träumner, K., Kottmeier, C., Corsmeier, U., and Wieser, A.: Convective boundary-layer entrainment: short
603 review and progress using doppler lidar, *Bound.-Lay. Meteorol.*, 141, 369–391,
604 <https://doi.org/10.1007/s10546-011-9657-6>, 2011.

605 Tucker, S. C., Senff, C. J., Weickmann, A. M., Brewer, W. A., Banta, R. M., Sandberg, S. P., Law, D. C., and
606 Hardesty, R. M.: Doppler lidar estimation of mixing height using turbulence, shear, and aerosol profiles,
607 *J. Atmos. Ocean. Tech.*, 26, 673–688, <https://doi.org/10.1175/2008JTECHA1157.1>, 2009.

608 Van Der Kamp, D. and McKendry, I.: Diurnal and seasonal trends in convective mixed-layer heights
609 estimated from two years of continuous ceilometer observations in Vancouver, BC, *Bound.-Lay.*
610 *Meteorol.*, 137, 459–475, <https://doi.org/10.1007/s10546-010-9535-7>, 2010.

611 Yang, T., Wang, Z., Zhang, W., Gbaguidi, A., Sugimoto, N., Wang, X., Matsui, I., and Sun, Y.: Technical
612 note: Boundary layer height determination from lidar for improving air pollution episode modeling:
613 development of new algorithm and evaluation, *Atmos. Chem. Phys.*, 17, 6215–6225,
614 <https://doi.org/10.5194/acp-17-6215-2017>, 2017.

615 Yates, D. N., Chen, F., Lemone, M. A., Qualls, R., Oncley, S. P., and Gross, R. L.: A cooperative
616 atmosphere-surface exchange study (CASES) dataset for analyzing and parameterizing the effects of
617 land surface heterogeneity on area-averaged surface heat fluxes, *J. Appl. Meteorol.*, 40,
618 [https://doi.org/10.1175/1520-0450\(2001\)040<0921:ACASES>2.0.CO;2](https://doi.org/10.1175/1520-0450(2001)040<0921:ACASES>2.0.CO;2), 2001.

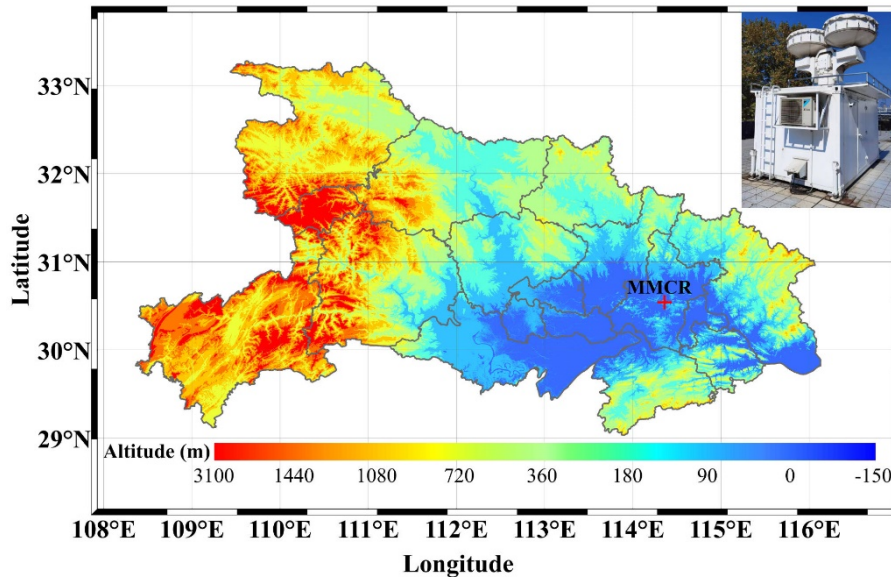
619 Zhang, H., Zhou, X., Zou, J., Wang, W., Xue, L., Ding, Q., Wang, X., Zhang, N., Ding, A., Sun, J., and

620 Wang, W.: A review on the methods for observing the substance and energy exchange between
621 atmosphere boundary layer and free troposphere, *Remote Sens.-Basel*, 15, 5397,
622 <https://doi.org/10.3390/rs15225397>, 2018.

623 Zhang, J., Guo, J., Li, J., Zhang, S., Tong, B., Shao, J., Li, H., Zhang, Y., Cao, L., Zhai, P., Xu, X., and Wang,
624 M.: A Climatology of merged daytime planetary boundary layer height over China from radiosonde
625 measurements, *J. Geophys. Res.-Atmos.*, 127, e2021JD036367, <https://doi.org/10.1029/2021JD036367>,
626 2022.

627 Zhang, M., Tian, P., Zeng, H., Wang, L., Liang, J., Cao, X., and Zhang, L.: A comparison of wintertime
628 atmospheric boundary layer heights determined by tethered balloon soundings and lidar at the site of
629 SACOL, *Remote Sens.-Basel*, 13, 1781, <https://doi.org/10.3390/rs13091781>, 2021.

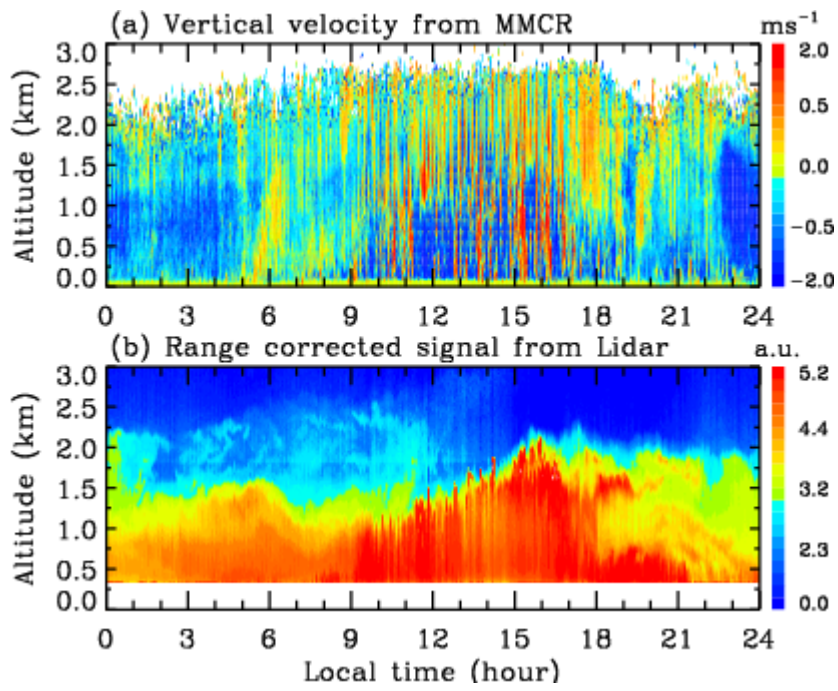
630 Zhang, Y., Zhang, S., Huang, C., Huang, K., Gong, Y., and Gan, Q.: Diurnal variations of the planetary
631 boundary layer height estimated from intensive radiosonde observations over Yichang, China, *Sci.*
632 *China Technol. Sc.*, 57, 2172–2176, <https://doi.org/10.1007/s11431-014-5639-5>, 2014.



633

634 **Figure 1.** Topographic elevation map of Hubei Province and Ka-band MMCR located in Wuhan University

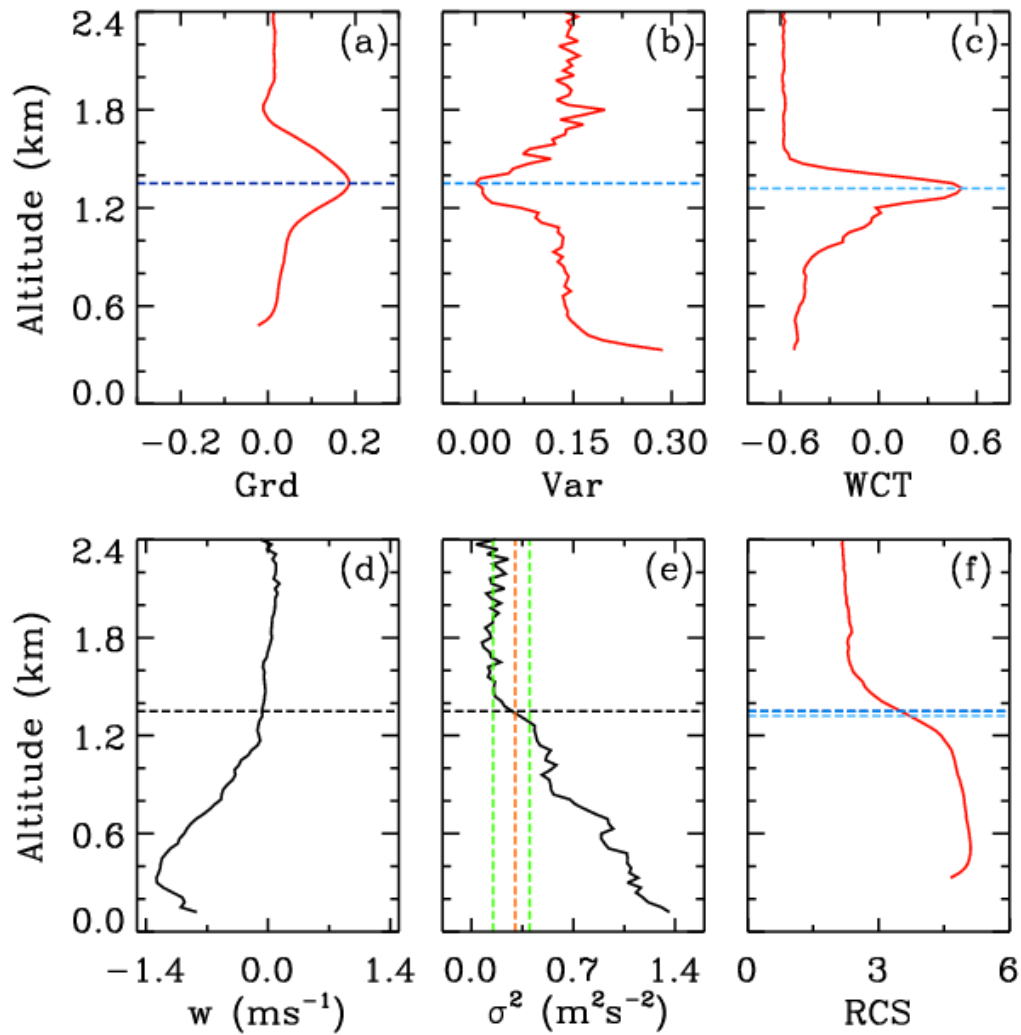
635 (30.54°N, 114.36°E). The red crisscross denotes the site of MMCR.



636

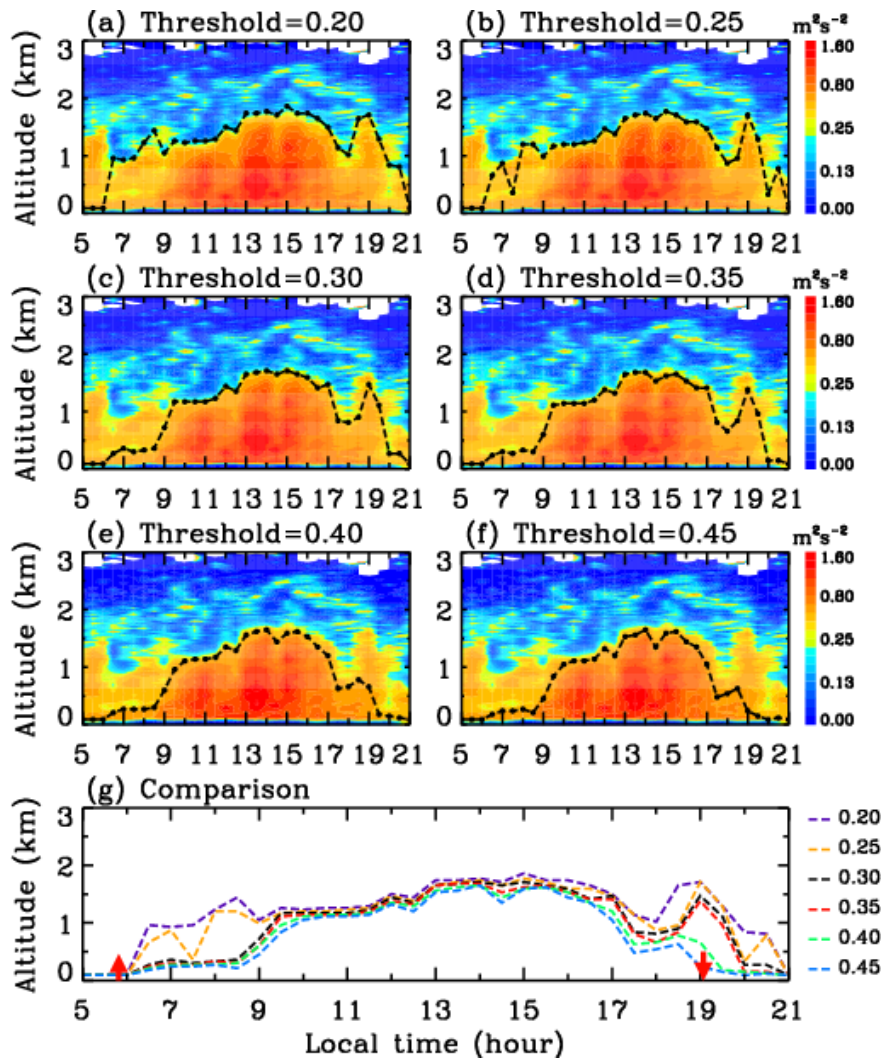
637 **Figure 2.** Time-height section of (a) vertical velocity from MMCR and (b) RCS from lidar on 15 August

638 2020.



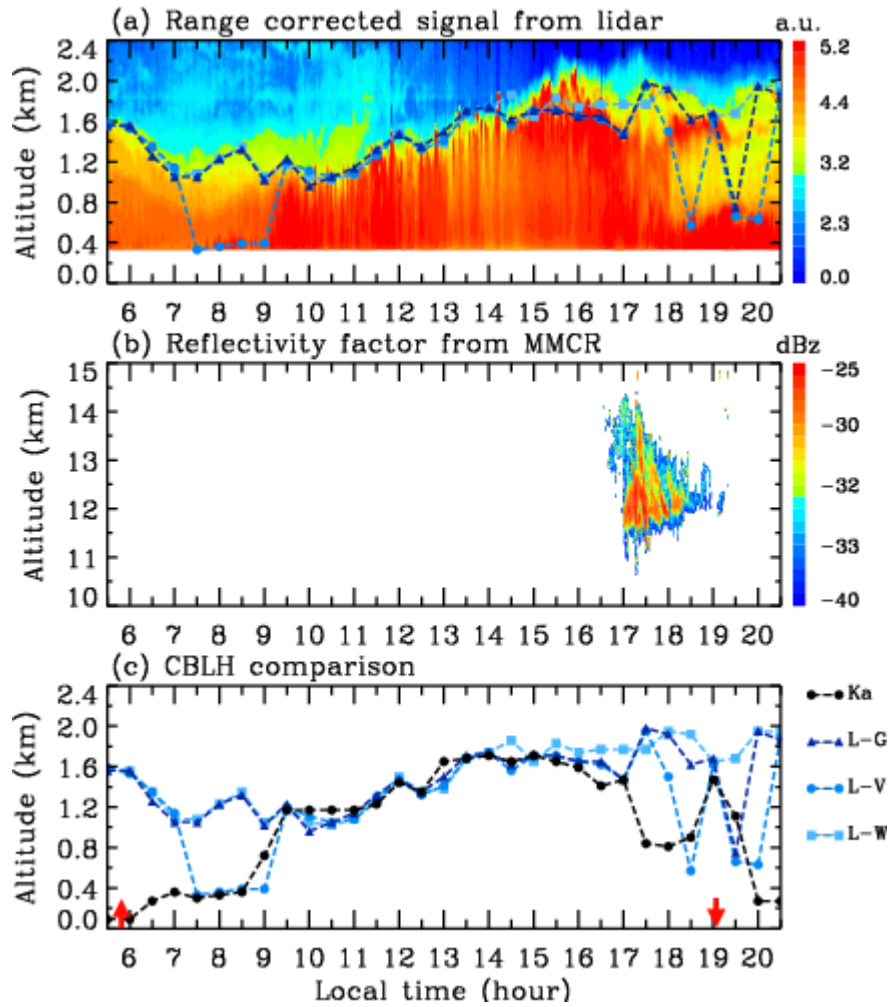
639

640 **Figure 3.** Profiles of (a) RCS gradient, (b) variance, (c) WCT and (f) RCS from lidar, and (d) vertical
 641 vertical velocity and (e) its variance from MMCR between 12:15 and 12:45 LT on 15 August 2020. In these panels,
 642 the horizontal lines in different colors represent the CBLH determined by different methods. In Panel 3e, the
 643 orange vertical line denotes the selected threshold of $0.3 \text{ m}^2 \text{ s}^{-2}$, and the two green vertical lines correspond
 644 to the variances of 0.15 and $0.4 \text{ m}^2 \text{ s}^{-2}$, respectively.



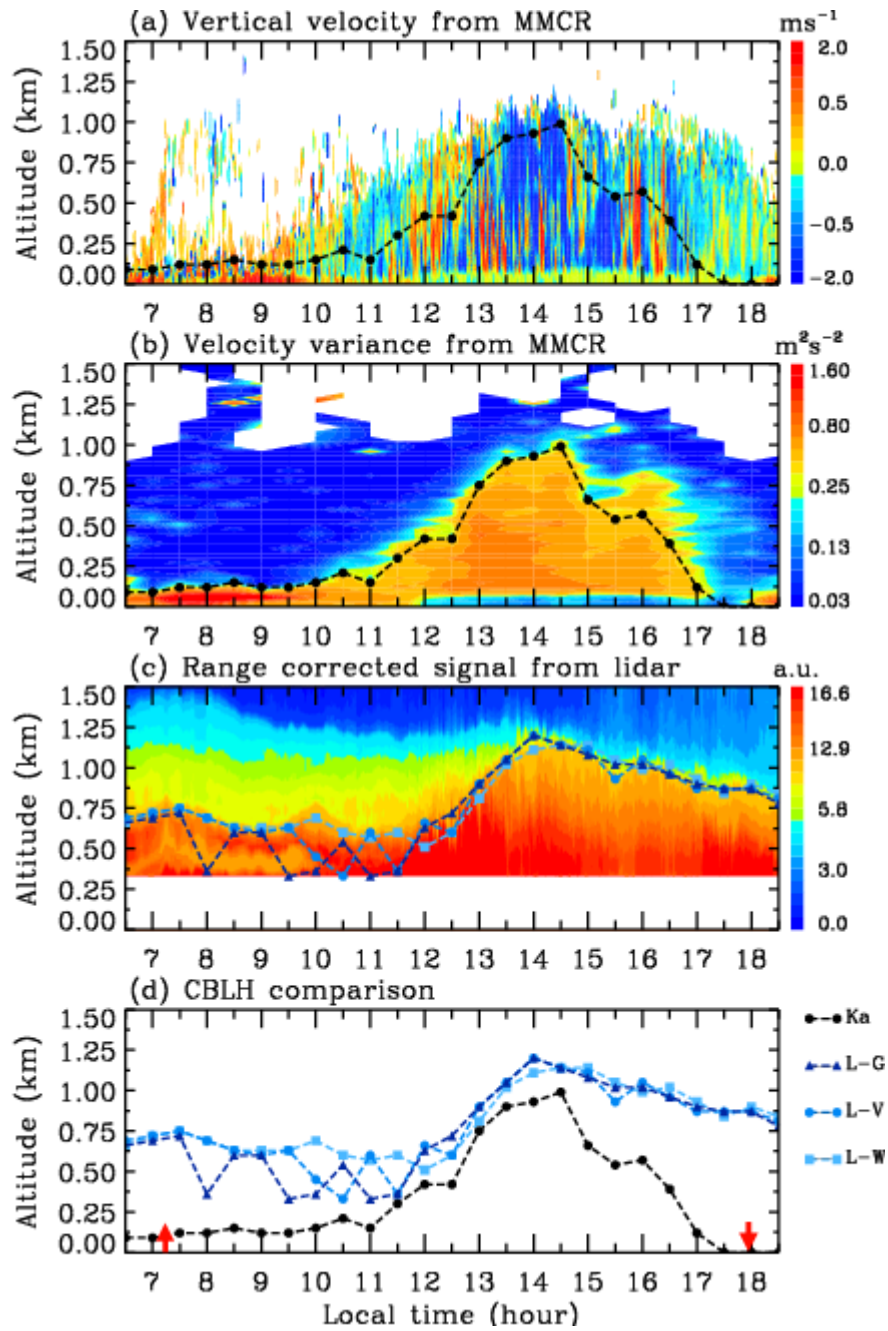
645

646 **Figure 4.** CBLHs derived from thresholds of (a) 0.2, (b) 0.25, (c) 0.3, (d) 0.35, (e) 0.4 and (f) 0.45 $\text{m}^2 \text{s}^{-2}$
 647 superimposed over vertical velocity variance (color shading) from MMCR on 15 August 2020, and (g) their
 648 comparison. In Panel 4g, the two red arrows denote the time of sunrise and sunset at 05:50 and 19:05,
 649 respectively.



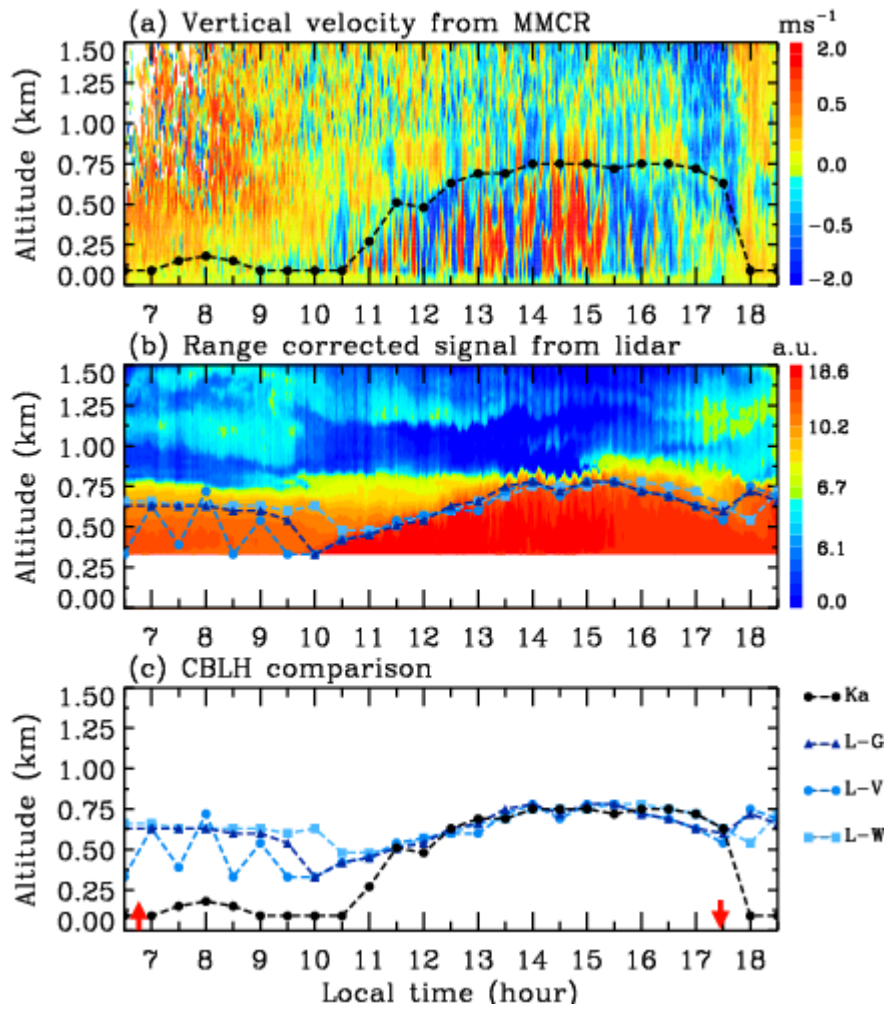
650

651 **Figure 5.** (a) Evolution of CBLH derived from RCS gradient, variance and WCT superimposed over lidar
 652 RCS (color shading) on 15 August 2020, (b) reflectivity factor from MMCR, and (c) comparison of CBLHs
 653 derived from MMCR and lidar observations. The black dash curve with circle (Ka) denotes the CBLH
 654 determined by the variance threshold of $0.3 \text{ m}^2 \text{ s}^{-2}$ in the Ka-band MMCR observation, while the dark blue,
 655 blue and light blue dash curves with triangle (L-G), circle (L-V) and square (L-W) represent the CBLH
 656 determined by the gradient, variance and WCT in the lidar measurement, respectively. In Panel 5c, the two
 657 red arrows denote the time of sunrise and sunset at 05:50 and 19:05, respectively.



658

659 **Figure 6.** Distributions of (a) vertical velocity and (b) its variance from MMCR and (c) lidar RCS on 31
 660 January 2020 with retrieved CBLH, and (d) comparison of CBLHs derived from MMCR and lidar
 661 observations. The threshold of vertical velocity variance from the MMCR is $0.3 \text{ m}^2 \text{ s}^{-2}$. In Panel 6d, the two
 662 red arrows denote the time of sunrise and sunset at 07:15 and 17:57, respectively.



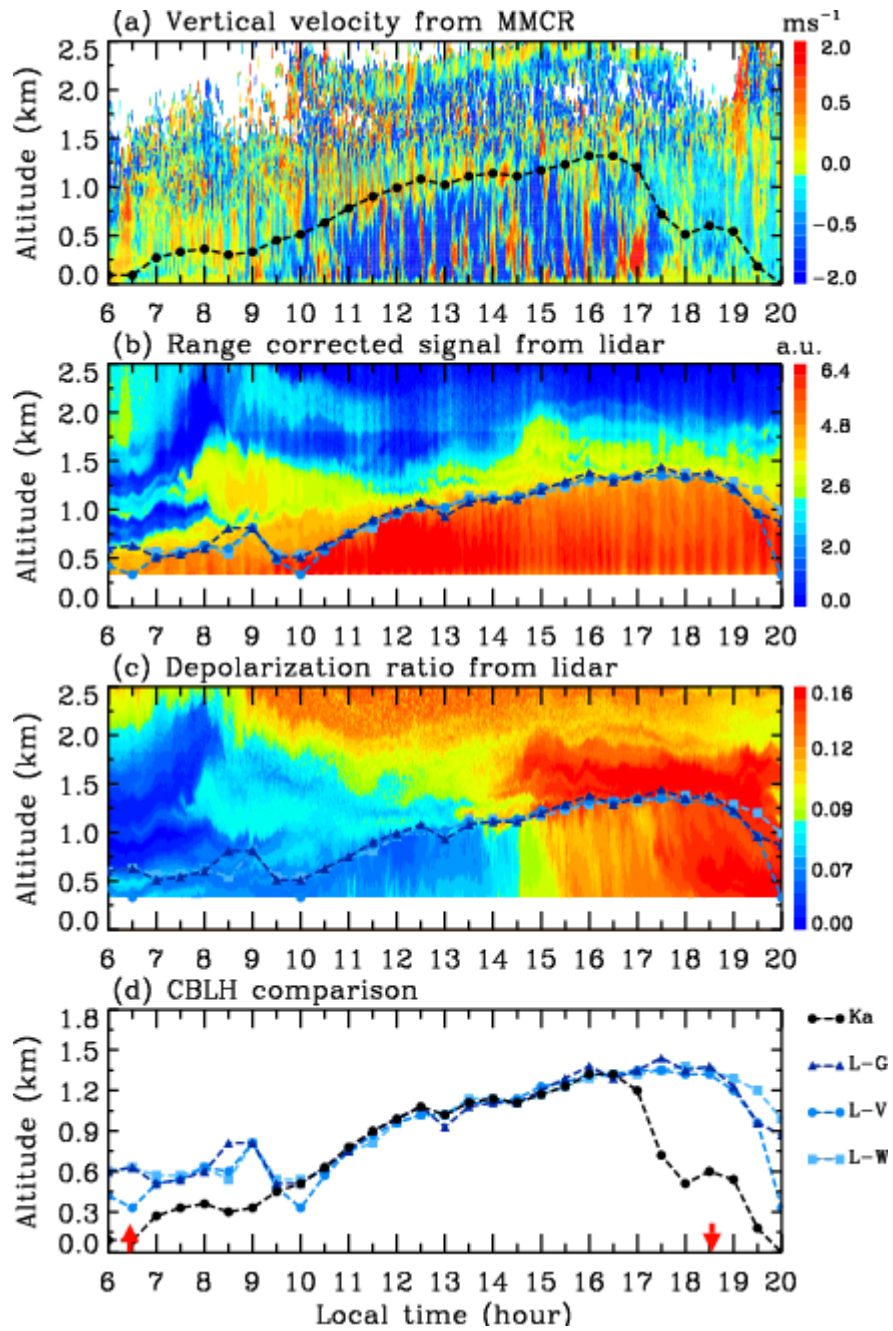
663

664 **Figure 7.** Distributions of (a) vertical velocity from MMCR and (b) lidar RCS on 12 November 2020 with

665 retrieved CBLH, and (c) comparison of CBLHs derived from MMCR and lidar observations. The threshold

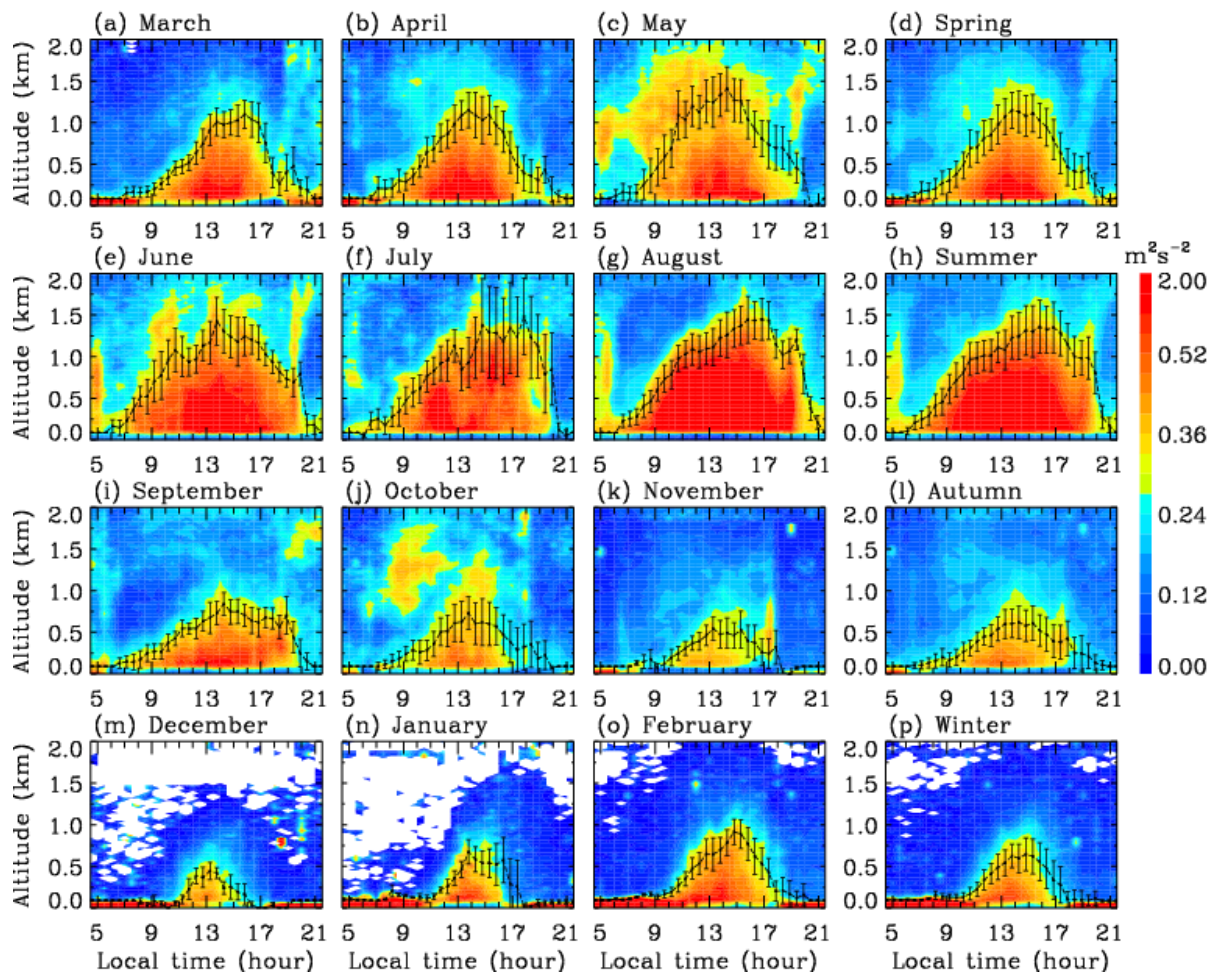
666 of vertical velocity variance from the MMCR is $0.3 \text{ m}^2 \text{ s}^{-2}$. In Panel 7c, the two red arrows denote the time of

667 sunrise and sunset at 06:47 and 17:27, respectively.



668

669 **Figure 8.** Distributions of (a) vertical velocity from MMCR and lidar (b) RCS and (c) depolarization ratio
 670 on 19 March 2020 with retrieved CBLH, and (d) comparison of CBLHs derived from MMCR and lidar
 671 observations. The threshold of vertical velocity variance from the MMCR is $0.3 \text{ m}^2 \text{ s}^{-2}$. In Panel 8d, the two
 672 red arrows denote the time of sunrise and sunset at 06:27 and 18:34, respectively.



673

674 **Figure 9.** Monthly and seasonal mean values and statistical standard deviations of CBLH estimated by
 675 threshold of vertical velocity variance from MMCR. The variance threshold is $0.3 \text{ m}^2 \text{ s}^{-2}$, and the color
 676 shading denotes the variance distribution. The months and seasons are marked above the corresponding
 677 panels, respectively.